Electrodeposition of Ru onto Ru and Au Seed Layers from Solutions of Ruthenium Nitrosyl Sulfate and Ruthenium Chloride

[1]Ryan Gusley, [2]Quintin Cumston, [2]Kevin R. Coffey, [1]Alan C. West, [3]Katayun Barmak

[1] Department of Chemical Engineering, Columbia University, New York, NY 10027

[2]Department of Materials Science and Engineering, University of Central Florida, Orlando, FL 32816

[3]Department of Applied Physics and Applied Mathematics, Columbia University, New York, NY 10027

Abstract

The electrodeposition of Ru was investigated from solutions of ruthenium(III) nitrosyl sulfate and ruthenium(III) chloride onto seed layers of epitaxial and polycrystalline Ru and epitaxial Au. Using both galvanostatic and potentiostatic deposition modes, metallic Ru was found to electrodeposit as a porous layer comprised of (0001) oriented Ru crystallites, the presence of which was discovered and confirmed by X-ray and scanning transmission and transmission electron microscope (S/TEM) analyses. This finding was independent of the Ru salt and seed layer used. Using X-ray reflectivity (XRR), the average film density ρ_{eff} of the porous electrodeposited Ru layer was measured as less than the density of bulk Ru $\rho_{Ru,bulk}$ (14.414 g/cm^3). Increasing the magnitude of the applied current density from -100 μA/cm^2 to -10 mA/cm^2 in solutions of Ru nitrosyl sulfate increased the ρ_{eff} from 7.4 g/cm^3 to 9.7 g/cm^2 while the current efficiency decreased from 9.4% to 4.3%.

Metallic Ru has applications in several industries, most notably in catalysis and in microelectronics. In catalysis, Ru is used in direct methanol fuel cells (DMFCs)[1–3] and for the conversion of CO and CO_2 to methanol.[4,5] For these purposes, this rare, Pt-group transition metal shows exceptionally high activity, both on its own[4] and as an alloy with Pt which is added as a solution to avoid the CO poison of the catalyst.[3] In microelectronics, Ru has been investigated as a diffusion barrier layer in electronic interconnects on IC chips[6–9] and, more recently, is considered a promising metal candidate to replace polycrystalline Cu interconnects at the lower levels of metallization where interconnect dimensions are the smallest.[10–12] Ru is expected to possess a lower resistivity than Cu at nano-scale dimensions due to its smaller electron mean free path, despite having higher values of bulk resistivity than Cu.[12,13] Additionally, with the knowledge that electron scattering at grain boundaries is a major contributor to the resistivity increase of metallic interconnects,[14,15] there has been focus on the fabrication of single crystal interconnects grown epitaxial to single crystal seed layers.[10,16–19] Recently, Co has been shown to electrodeposit as a single crystal epitaxial to seed layers of Ru(0001) despite a large lattice mismatch of 7.9%.[10,16,17] Thus, Ru, which has an expected 0% misfit strain with the Ru(0001) seed layer, was considered to have a high likelihood to deposit as a single crystal as well.

In the academic and patent literature, Ru is most commonly electrodeposited from solutions containing salts of Ru nitrosyl chloride,[20] Ru nitrosyl nitrate,[21,22] Ru nitrosyl sulfamate,[23] Ru nitroso chloride,[24] Ru chloride,[25–27] among others[28–30] from aqueous electrolytes, ionic liquids,[26,31] and water-in-salt electrolytes.[32] Several commercial baths exist as well.[33,34] In academic literature, it has been reported that the density of electroplated Ru is generally less than the expected theoretical value for bulk Ru.[34] Additionally, Wang et al. note that Ru electrodeposits as nano-

sized crystallites referred to as ultra-small grains from the commercial electrolyte produced by Technic Inc.[33]

In this work, Ru films electrodeposited from Ru nitrosyl sulfate were investigated with X-ray and electron microscopy techniques. The Ru films were electrodeposited onto epitaxial Ru(0001) and polycrystalline Ru. Additionally, the Ru films were electrodeposited from $RuCl_3$ salts and onto epitaxial Au(111). After the analyses, it was determined that Ru electrodeposits as a porous layer composed of (0001) oriented Ru crystallites, where the average density of the layer, ρ_{eff}, is dependent on the applied current density, *i,* which the film is deposited with.

Methodology

Experiments.-Three different seed layers were used for the electrodeposition of Ru layers, namely epitaxial Ru(0001), polycrystalline Ru, and epitaxial Au(111). The single crystal Ru films were deposited following the procedure outlined by Ezzat *et al*.[11] To summarize, the epitaxial 60 nm-thick Ru(0001) films were deposited onto c-plane sapphire, Al_2O_3(0001), by ultra-high vacuum (UHV) sputter deposition at 500°C with a base pressure in the low 10^{-8} Torr range. Subsequently, the Ru layers were *ex situ* step annealed in one atmosphere of flowing Ar/3% H_2. Once the initial anneal temperature of 350°C was stable for 30 minutes, the anneal proceeded in steps of 100°C up to 950°C, with each temperature held for 30 minutes. Next, the temperature was decreased by steps of 100°C until 150°C was reached, with each temperature held for 60 minutes. The polycrystalline Ru films were deposited by sputter deposition at room temperature and a minimum base pressure of 5×10^{-7} Torr. The 100 nm-thick Ru film was grown atop 4 nm-thick TaN deposited onto SiO_2/Si through reactive sputtering in Ar-N_2 at room temperature and a minimum base pressure of 5×10^{-7} Torr. The 20 nm-thick single crystal Au(111) film was deposited onto 20 nm Ru(0001)/Al_2O_3(0001) by UHV sputter deposition at 200°C with a base pressure in the low

10^{-8} Torr range. The 20 nm-thick Ru(0001) was deposited by UHV sputter deposition at 700°C with a base pressure in the low 10^{-8} Torr range.

The sapphire wafers with deposited layers of Ru and Au were laser cut into coupons and electroplating tape was used to limit the geometric surface area of the coupon that was exposed to the electrolyte. To prepare the Ru and Au films for experimentation, the coupons were rinsed several times with acetone, isopropyl alcohol, and 18.2 MΩ-cm de-ionized (DI) water. For the Ru seed layers, a potentiostatic hold at -0.8 V vs. Ag/AgCl in 50 mM sulfuric acid (H_2SO_4, Sigma-Aldrich) for 120 s was employed to cathodically reduce the native surface oxides from the Ru layer.[35]

The Ru electrodeposition solution contained 2 g/L (3.6 mM) ruthenium(III) nitrosyl sulfate ($[Ru(NO)]_2(SO_4)_3$, Alfa Aesar, 99.99%) and 20 g/L (0.204 M) sulfuric acid (H_2SO_4, Fisher Chemical, TraceMetal™ Grade). The pH of this solution was measured as 0.7. Ru chloride electrodeposition solution contained 10 mM Ru(III) chloride ($RuCl_3$, ACROS Organics, 99.9%) and 0.1 M hydrochloric acid (HCl, Fisher Chemical, TraceMetal™ Grade). All solutions were purged with argon (Ar) for a minimum of one hour prior to electrochemical experiments to remove dissolved oxygen. The aqueous solutions were made with 18.2 MΩ-cm deionized (DI) water (Direct-Q 3 UV-R, Millipore).

The Ru films were electrodeposited under both galvanostatic and potentiostatic control onto the Ru(0001), polycrystalline Ru, and Au(111) seed layers. During the electrodeposition of Ru, the solution was stirred using a magnetic stir bar rotating at 150 RPM and Ar was flowed in the headspace of the electrochemical cell. The electrodeposition set-up was operated as a three electrode cell with a Ru or Au film as the working electrode, a platinum (Pt)-wire counter electrode, and an Ag/AgCl (Hach) reference electrode with an internal solution of saturated KCl

and AgCl (E = 0.199 V vs. NHE). All potentials are cited against a saturated Ag/AgCl reference electrode unless otherwise stated. A Metrohm μAutolab Type III potentiostat was used for all electroanalytical measurements.

X-ray diffraction (XRD) and X-ray reflectivity (XRR) scans were performed using a Rigaku SmartLab 3 kW XRD. The machine was operated at 40 mA and 45 kV with a Cu source (λ = 1.54 Å) using parallel beam optics. The XRR measurements were obtained using a Ge(220) 2-bounce monochromator. Before performing the *θ-2θ* and XRR scans, an alignment of the instrument and sample was performed using the instrument's AutoAlign^{TM} function. The X-ray incident slit (IS) size was selected to ensure the reflectivity of nearly the entire surface area of the electrodeposited Ru was measured. Thus, the measurement of thickness d, film density ρ_{eff}, and RMS roughness σ are average values over the entire electrodeposited area. XRR curves were fit using the Rigaku SmartLab software, which makes use of the Parratt formalism for reflectivity.[36]

The electrodeposited Ru thin films were imaged in cross section using an FEI Talos F200X scanning transmission/ transmission electron microscope (S/TEM) operating at 200 kV. The electron transparent cross sections were prepared by focused ion beam (FIB) milling in an FEI Helios NanoLab 660 dual beam instrument. The sample cross sections were prepared in the direction parallel to the $\{10\bar{1}0\}$ planes of the sapphire, thus, the $\{11\bar{2}0\}$ planes of Ru because of the 30° rotation between epitaxial Ru and sapphire.[18]

Fitting and Analysis of X-ray Reflectivity Curves.- XRR is a versatile technique commonly used in the semiconductor industry for the precise measurement of the thickness d, density ρ_{eff}, and RMS roughness σ of films below 500 nm of thickness.[37] To fit the XRR curves obtained from Ru films electrodeposited onto the 60 nm-thick Ru(0001) seed layers, the curves were first obtained

on the Ru(0001) seed layers with no electrodeposited layers and a fit was performed. The density of Al_2O_3 $\rho_{Sapph,bulk}$ and Ru density $\rho_{Ru,bulk}$ were fixed as 3.989 g/cm^3 and 12.414 g/cm^3, respectively,[18,38] with the free fitting parameters chosen as Ru film thickness d_{seed}, root mean square (RMS) roughness of the top surface of the Ru layer σ_{seed}, and of the interface between Ru and sapphire, $\sigma_{seed-sapphire}$. Ru was then electrodeposited onto the seed layer, and another XRR curve was collected. Finally, a second fit was performed where the d_{plated}, ρ_{eff}, and σ_{plated} of the electrodeposited Ru layer were selected as the free fitting parameters. The parameters of the seed layers, namely the thickness d_{seed} of the Ru(0001) seed layer as well as the RMS roughness σ_{seed} at the surface of the Ru seed layer and at the interface of the Ru layer and sapphire substrate $\sigma_{seed-sapphire}$, are set from the previous XRR fit.

To determine the average film density ρ_{eff} of Ru electrodeposited onto polycrystalline Ru seed layers, a calibration curve relating ρ_{eff} to the critical angle of X-ray total reflection Θ_c was generated. At sufficiently small angles during the XRR measurement, total reflection of the incident X-rays occurs, and all X-rays are reflected from the surface of the thin-film. The critical angle for total reflection θ_c is the angle at which the incident X-rays begin to penetrate the sample. The θ_c is taken as the angle at which the measured intensity is half of the maximum recorded intensity.[39–41] The density of a sample is proportional to the critical angle θ_c from the measured XRR curve, where a larger θ_c indicates a greater density.[37,42] The value of θ_c can be calculated using the dispersion aspect of wave-matter interaction δ.[41,42] When X-ray absorption is disregarded:

$$\theta_c = \sqrt{2\delta} \quad [1]$$

where δ is calculated as:

$$\delta = \left(\frac{r_e \lambda^2}{2\pi} \right) N_0 \rho \frac{\sum_i x_i \left(Z_i + f_i^{'} \right)}{\sum_i x_i M_i}. \quad [2]$$

In this relationship, r_e is the classical radius of an electron (2.818×10^{-9} m), λ is the Cu X-ray wavelength (0.15406 nm), N_0 is Avogadro's number, ρ is the film density, x_i is the atomic ratio of the i^{th} atom, f_i' is the atomic scattering factors of species i, and M_i is the atomic mass of species i. Therefore, the relationship between θ_c and the effective density of the film ρ_{eff} is:

$$\theta_c \propto \sqrt{\rho_{eff}}. \quad [3]$$

Using a calibration curve created from XRR curves obtained on wafers of sapphire (3.989 g/cm^3) and thin-film samples of sputter deposited copper (8.93677 g/cm^3) and Ru (12.414 g/cm^3), the ρ_{eff} of the electrodeposited Ru samples was estimated through the measurement of θ_c. The calibration curve is included in the supplemental information for this manuscript (Fig. S1). XRR curves obtained on the 100 nm-thick polycrystalline Ru and 60 nm-thick Ru(0001) seed layers indicate that the layers have the same θ_c, hence, ρ (Fig. S2).

Results and Discussion

This section is structured as follows. First, electrochemical experiments and results pertaining to the Ru electrodeposition reaction from solutions of dissolved Ru nitrosyl sulfate are presented. Next, results from X-ray and microscopy analyses performed on the electrodeposited Ru films are discussed and information regarding the Ru layer density ρ_{eff} and microstructure is

provided. Finally, sample annealing and variations of the electrolyte and seed layer are investigated for their impact on the ρ_{eff} of the electrodeposited Ru films.

Figure 1a shows the result of two linear sweep voltammograms (LSVs) collected on a 60 nm-thick Ru(0001) film from solutions of 20 g/L sulfuric acid with and without 2 g/L ruthenium(III) nitrosyl sulfate. The scans were performed to determine the reduction potential of the dissolved Ru metal ion species in the electrodeposition solution as well as the amount of hydrogen evolution occurring simultaneous to the electrodeposition reaction. In both LSVs, the potential was scanned in the negative direction at 2 mV/s from open circuit potential (OCP). The pH of each solution was measured as 0.7, and the Nernst reduction potential for the hydrogen evolution reaction (HER) at this pH is calculated as $U_{H_2|H^+} = -0.24\ V$ vs Ag/AgCl. In agreement with this calculated value, the magnitude of the reduction current density from the scan performed in the absence of Ru salt begins to increase around -0.24 V, however, significant rates of hydrogen evolution are not observed on the Ru(0001) film until greater overpotentials. Using the same Ru coupon, 2 g/L $[Ru(NO)]_2(SO_4)_3$ was dissolved in 20 g/L H_2SO_4 (pH = 0.7) and the scan was repeated. In this solution, the reduction current density increases at potentials negative of -0.2 V vs. Ag/AgCl. The pH is constant between the two solutions, therefore, this current density is attributed the reduction of the ionic Ru species in solution, $RuNO^{3+}$.[43,44] The reduction of ruthenium from Ru-nitrosyl complex salts was determined by cyclic voltammetry and chronopotentiometry studies to proceed as multiple electron transfer steps where the Ru(III) ionic species is reduced until metallic Ru^0 is deposited.[21,45,46] The LSV shows no sign of diffusion limitation despite the low concentration (3.6 mM) of Ru salt.

Figure 1b shows the resulting potential transients from Ru electrodeposited galvanostatically at current densities from -100 μA/cm^3 to -5 mA/cm^2. The current densities were

passed for a charge density of 0.7 C/cm^2 and the depositions were performed with a stir bar rotation of 150 rotations per minute (RPM). When compared with the LSV from Fig. 1a, the overpotentials are less for all current densities due to the convection from the stir bar agitation. The recorded potentials are unstable with time, yet applied current density is nearly constant with a standard deviation between 5 μA/cm^2 and 15 μA/cm^2. This phenomenon was independent of solution agitation, equipment, and seed layer used, thus, the fluctuation in potential appears to be caused by the Ru metal ion reduction reactions taking place on the electrode. The color of the electrodeposited films differed from that of the sputter deposited Ru seed layer. At smaller magnitudes of current densities, the film looked brown with a burnt appearance where the sputter deposited Ru thin film was a silver, metallic color. Electrodeposition at current densities negative of -1.25 mA/cm^2 more closely resembled the color of the Ru seed layer. Light optical micrographs of the Ru(0001) seed layer and electrodeposited Ru films are provided in the supplementary information for this manuscript (Fig. S3).

In a procedure detailed below, X-ray reflectivity (XRR) curves were obtained for each of the electrodeposited Ru films which provided a measurement of the thickness d_{plated} and average density ρ_{eff} of the electrodeposited Ru layers. In this manuscript, current efficiency ε is taken as the amount of Ru deposited (calculated in mass) over the theoretical maximum amount of Ru deposited from the total charge density passed q_{tot} (C/cm^2). Using q_{tot}, electrodeposited Ru film thickness d_{plated}, and ρ_{eff}, the current efficiency ε (%) of the complete reduction of $Ru(NO)^{3+}$ to Ru^0 was calculated by:

$$\varepsilon = \frac{3F\rho_{eff}d_{plated}}{q_{tot}M_{Ru}} \times 100\% \qquad [4]$$

where F is Faraday's constant and M_{Ru} is the atomic mass of Ru. Therefore, HER and the partial reduction of the complexed Ru metal ion species, i.e.:

$$Ru(NO)^{3+} + e^- \leftrightarrow Ru(NO)^{2+}, \quad [5]$$

reduce the current efficiency.[21] The current efficiency values are plotted as a function of applied current density in Fig. 1c. In all cases, the current efficiencies are less than 10%. Increasing the magnitude of current density from -100 μA/cm^2 to -10 mA/cm^2 yielded a steady decline in current efficiency from 9.4% to 4.3%. The LSVs, performed at quasi-steady state, suggest that minimal hydrogen evolution occurs during Ru electrodeposition at current densities up to i = -10 mA/cm^2. At the potential where -10 mA/cm^2 is achieved in the Ru electrodeposition solution, the HER current from the baseline solution is -450 μA/cm^2, accounting for under 5% of the total applied i. The low current efficiencies observed during Ru electrodeposition from this particular solution, then, are hypothesized to be due to the diffusion and escape of $Ru(NO)^{2+}$ (equation [5]) and perhaps other reduced species into the bulk solution resulting in the incomplete reduction of $Ru(NO)^{3+}$ to Ru^0.

The X-ray and electron microscopy studies outlined below indicate that the electrodeposited Ru did not deposit as a single crystal, but rather as a porous Ru layer. This porosity causes the average density of the layer to be less than a layer of fully dense Ru. The average density over the entire electrodeposited Ru layer, consisting of Ru crystallites and voids, will be referred to as the effective density ρ_{eff}. Following this notation, it can be said that the electrodeposited Ru layer has a lower ρ_{eff} (higher porosity) than $\rho_{Ru,bulk}$. Previous studies have demonstrated the epitaxial electrodeposition of Co as a single crystal onto seed layers of 60 nm-thick Ru(0001) despite a large misfit strain of 7.9%.[10,16,17] Ru has 0% misfit with the Ru(0001) seed layer, yet does not electrodeposit as a contiguous, dense single crystal layer. One reason why

Ru does not electrodeposit as a contiguous, dense layer may be that the Ru metal ions are reducing from a complexed species. The reduction process involves the adsorption of the Ru species to the seed layer surface, reduction of the Ru species, and eventual desorption of the ligand. This process may inhibit the electrodeposition of a contiguous Ru layer. Further, it is unlikely the co-evolution of hydrogen is the main contributing source of the lower ρ_{eff}. While HER has been shown to cause porosity in electrodeposited films,[47] the Ru film electrodeposited at -100 μA/cm^2 possesses the greatest porosity and the lowest ρ_{eff}, which is quantified below, yet the electrode potential remains positive of $U_{H_2|H^+}$ throughout the course of the galvanostatic deposition. Thus, the thermodynamics of HER support this claim. Ru electrodeposition does take place in the potential regime of H underpotential deposition (H_{UPD}) and OH adsorption. Adsorbed H and OH atoms have been said to affect the nucleation and growth of metals[48–51] and to decrease surface diffusion of metal adatoms resulting in the deposition of many small crystals.[52] Previous studies, however, suggest that the presence of H_{UPD} and OH^- adsorption did not affect the quality of electrodeposited Co grown epitaxial to Ru(0001).[16,17] The nucleation density of electrodeposited Ru and lower atomic mobility of the Pt group metal may also impact the density of the deposit.

A symmetric θ-2θ X-ray diffractogram was collected between 5° and 100° on electrodeposited Ru. The scan was performed on the 60 nm-thick Ru(0001) seed layer before and after Ru electrodeposition at -100 μA/cm^2 for a charge density of q = 0.7 C/cm^2 to detect the presence of additional Ru crystal orientations or Ru oxide species. Fig. 2a features the entire diffractogram with intensity plotted on a logarithmic scale. The thickness of the electrodeposited Ru layer, determined by an analysis of the cross-section transmission electron microscopy (TEM) images below, is about 30 nm. Peaks measured at 41.681°, 41.786°, and 42.187° are reflections

from the $k\alpha_1$ and $k\alpha_2$ of Al_2O_3(0006) and from Ru(0002), respectively. Fig. 2b shows a section of this diffractogram from 40.5° to 43.5° with intensity plotted on a linear scale. The intensity of the Ru(0002) peak from the scan performed on the electrodeposited Ru layer is larger than the peak intensity from the scan of just the Ru(0001) seed layer obtained prior to electrodeposition. This intensity increase suggests a larger volume of (0001) orientated Ru after Ru electrodeposition on the seed layer. In addition to the reflections from $k\alpha_1$, $k\alpha_2$, and $k\beta$ of Al_2O_3(00012) and Ru(0004), several other reflections are present which are observed on both the Ru(0001) seed layer and the seed layer with electrodeposited Ru (with exception of the peak at 69.5° which is present only from the seed layer). These peaks were found to disappear and re-appear when changing the ω offset (Fig. S4) which suggests that these reflections are generated by a combination of double diffraction from the single crystal Ru and sapphire layers or from defects within the sapphire substrate. The XRD patterns of Fig. 2 suggest that Ru was not electrodeposited with a random orientation or as an oxide.

Figure 3a shows the XRR curves obtained on the 60 nm-thick Ru(0001) seed layer before and after Ru electrodeposition. Ru was electrodeposited at -100 $\mu A/cm^2$ with a charge density of 0.7 C/cm^2. The 2θ value corresponding to $2\theta_c$ is indicated on Fig. 3a. As the X-rays penetrate the sample, a signal is received from each layer that possesses a different refractive index n, where n corresponds to the mass-density of the layer. The oscillations observed in the curve are Kiessig (interference) fringes from the layers, where the period of oscillations is related to the thickness of the layer.[37,42,53] Had the electrodeposited Ru layer grown as a contiguous, dense single crystal layer onto the Ru(0001) seed layer, a change in the period of oscillations would have occurred. At higher 2θ, no such change is observed. Rather, the difference between the curves lies at smaller 2θ angles. Here, a different critical angle is observed as the intensity of the curve obtained on Ru

electrodeposited onto the Ru(0001) seed layer begins to decay at an angle smaller than on the XRR curve for the Ru(0001) seed layer. This indicates that the average density of the electrodeposited Ru layer is lower than that of the Ru(0001) seed layer. When scanned beyond $2\theta_c$, the curve begins to oscillate with a periodicity larger than that of the 60 nm-thick Ru seed layer. This periodicity is related to the thickness of the less dense electrodeposited Ru layer. As the scan angle increases and X-rays begin to penetrate the seed layer, the periodicity of oscillations begins to match that of the seed layer indicating that the thickness of this layer has not changed.

Figure 3b shows the measured XRR curve of Ru electrodeposited at -100 μA/cm^2 with the corresponding fit. The fit provides a measure of the average thickness d_{plated} and ρ_{eff} of the electrodeposited Ru layer in addition to the RMS roughness σ_{plated} at the surface of the Ru layer. From the fit, the thickness d_{plated}, ρ_{eff}, and σ_{plated} were found to be 28.6 ± 0.4 nm, 7.69 ± 0.05 g/cm^3, and 3.30 ± 0.05 nm, respectively. The quality of the fit, measured as R-factor, is 2.836%. This ρ_{eff} is considerably lower than the literature value for bulk Ru $\rho_{Ru,bulk}$, suggesting that the electrodeposited Ru layer is porous. The ratio of $\rho_{eff}/\rho_{Ru,bulk}$ is 0.62. Excellent agreement is observed between the average sample thickness obtained with XRR and the local thickness measured with cross-section TEM (d_{plated} = 28.9 ± 1.5 nm). This agreement suggests that the local electrodeposited film thickness is representative of the entire sample, and that this thickness is relatively constant over the coupon.

Figure 4a contains a low angle section of the XRR curves obtained on a 100 nm-thick polycrystalline Ru seed layer along with the polycrystalline Ru seed layer plus Ru layers electrodeposited at various current densities. The $2\theta_c$ for each curve is at the intersection of the

curve with the x-axis. The $2\theta_c$ of the polycrystalline Ru seed layer with an assumed density of $\rho_{Ru,bulk}$ (12.414 g/cm^3) is 0.961°. The $2\theta_c$ of all electrodeposited Ru samples is less than 0.961°, indicating a lower ρ_{eff}, with the smallest $2\theta_c$ belonging to the XRR curve obtained from Ru electrodeposited at -100 μA/cm^2. An increase in the magnitude of *i* yielded a greater value of $2\theta_c$, hence, ρ_{eff}. Each deposition was repeated in triplicate, and the ρ_{eff} of each film was determined through the measurement of $2\theta_c$. The ρ_{eff} is displayed as a function of current density in Fig. 4b. At current densities *i* more negative of -1.25 mA/cm^2 (i.e., magnitude of current > 1.25 mA/cm^2), no significant increase in ρ_{eff} was observed. A ρ_{eff} equal to $\rho_{Ru,bulk}$ was not achieved from this electrolyte with galvanostatic deposition.

Phase contrast cross-section TEM micrographs of Ru electrodeposited at -100 μA/cm^2 and -10 mA/cm^2 are presented in Figs. 5a-b. The films were deposited for 0.7 C/cm^2 onto 60 nm-thick Ru(0001). The electrodeposited Ru layer is above the Ru(0001) seed layer that was sputter deposited epitaxial to c-plane sapphire. A variation in contrast is observed between the two Ru layers. The local thickness of the Ru layer determined from cross section TEM is 28.9 ± 1.5 nm and 24.6 ± 2.5 nm for the layers electrodeposited at -100 μA/cm^2 and -10 mA/cm^2, respectively. The roughness of the Ru layer deposited at -10 mA/cm^2 appears greater than the layer deposited at -100 μA/cm^2. Nanobeam diffraction patterns from each of the Ru layers are shown in the inset of Fig. 5a. Electron diffraction from the Ru seed layer (yellow inset) shows a spot diffraction pattern indicating that the Ru seed layer is a single crystal.[54] The pattern from the electrodeposited layer resembles that of the seed layer, but with notably weaker spot intensities as a result of poor crystallinity when compared with the epitaxial, single crystal seed layer. The resemblance of the diffraction patterns of the electrodeposited Ru layer and the seed layer indicates that the plated

layer is also (0001) oriented. However, the higher-resolution image of the Ru layer electrodeposited at -10 mA/cm^2 in Fig. 5c shows that the electrodeposited Ru layer is composed of small crystallites that are slightly rotated or displaced relative to each other and thus give rise to the observed Moiré fringes.[54] These fringes should not be mistaken for atomic planes. The selected area electron diffraction (SAED) in the white inset of Fig. 5c shows the diffraction pattern from the electrodeposited layer. The diffraction pattern from the electrodeposited Ru layer is not a ring, which would indicate a randomly oriented polycrystalline film, but rather is composed of arcs surrounding the Ru diffraction spots. This again suggests that the electrodeposited Ru layer is crystalline but that has a distribution of its [0001] axis about the surface normal. The higher-resolution image of Fig. 5c also reveals that the electrodeposited Ru layer is porous consistent with the XRR result that the electrodeposited Ru film ρ_{eff} is less than $\rho_{Ru,bulk}$. Though the ρ_{eff} of the layer is less than $\rho_{Ru,bulk}$, it is important to note that the individual crystallites have the density of $\rho_{Ru,bulk}$. Thus, the inability of Ru to deposited epitaxially as a fully dense, single crystal layer appears to be the result of the electrolyte chemistry and reduction mechanism.

The porosity of the electrodeposited Ru layer is once again visible in the scanning transmission electron microscope (STEM) images in Fig. 6a-b. The high-angle annular dark-field (HAADF) STEM images highlight the mass-contrast in the layers. In both Ru films, the electrodeposited layers are primarily bright containing dark regions within. These dark areas indicate an absence of Ru. The results of an energy dispersive X-ray spectroscopy (EDS) line scan performed through the sample in the direction of the white arrows drawn onto the STEM images is represented in Fig. 6c. The scans, which start above the electrodeposited Ru layer and end within the sapphire substrate, detected a lower Ru signal from the electrodeposited layers than from the seed layer. This suggests that the ρ_{eff} of the electrodeposited Ru layers are lower than $\rho_{Ru,bulk}$ due

to the observed porosity. From the EDS line scan performed on the sample in Fig. 6a, the ratio of the Ru signal in the electrodeposited layer divided by the signal from the seed layer is ~0.52. This ratio is in fair agreement with the ratio of $\rho_{eff}/\rho_{Ru,bulk}$, determined as 0.62 from XRR. The cross-section of the sample electrodeposited at -10 mA/cm^2 is thinner in the electron beam direction than the sample deposited at -100 μA/cm^2, causing the film to appear to have a higher porosity. The Ru signal from the layer electrodeposited at -10 mA/cm^2 relative to the maximum Ru signal in the seed layer, however, is larger than the signal from the layer electrodeposited at -100 μA/cm^2. Therefore, the Ru layer electrodeposited at the more negative current density has a greater ρ_{eff} than the film deposited at -100 μA/cm^2.

Ru films electrodeposited onto Ru(0001) at -100 μA/cm^2, -5 mA/cm^2, and -10 mA/cm^2 (q = 0.7 C/cm^2) were annealed at 400° C for 30 minutes while flowing Ar/3% H_2 to observe changes in ρ_{eff}. This temperature was selected as it is within the thermal budget constraints for back-end-of-line (BEOL) processing during IC chip fabrication.[55] The temperature and time of anneal were selected as an example that is representative of a BEOL annealing treatment. A more comprehensive treatment would be addressed in process development and integration. For all samples, an increase in ρ_{eff} was measured after annealing. The sample electrodeposited at -5 mA/cm^2 experienced an 8.7% increase in ρ_{eff}. This change in ρ_{eff} induced a film thickness decrease from 25 nm to 22 nm and was accompanied by a 29% decrease in σ. The anneal did not result in the ρ_{eff} of the electrodeposited Ru layer reaching the value for $\rho_{Ru,bulk}$.

Potentiostatic deposition and modifications to the deposition electrolyte were used to investigate their effect on the ρ_{eff} of electrodeposited Ru. The electrolyte pH was changed by

reducing the sulfuric acid concentration. Ru was electrodeposited from several *i* between -100 μA/cm^2 and -10 mA/cm^2 from solutions of 2 g/L ruthenium nitrosyl sulfate and 10 g/L sulfuric acid with 10 g/L potassium sulfate (pH = 1.1) or 2 g/L ruthenium nitrosyl sulfate with 20 g/L potassium sulfate (pH = 3.2). Further changes were made to the electrolyte by increasing the Ru salt concentration of the original deposition solution from 2 g/L to 4 g/L. Additionally, from the original electrodeposition solution, Ru electrodeposition was performed from elevated temperatures of 40°C and 55°C. Finally, potentiostatic deposition was used instead of galvanostatic electrodeposition. None of the listed adjustments yielded the electrodeposition of Ru with a ρ_{eff} greater than 10 g/cm^3.

Ru films electrodeposited from solutions of 10 mM ruthenium chloride and 0.1 M hydrochloric acid possessed low ρ_{eff}, just as the films electrodeposited from the Ru nitrosyl sulfate bath. The highest ρ_{eff} of the Ru films electrodeposited from this solution was measured as 9.9 g/cm^2 when deposited with i = -2 mA/cm^2. Thus, the finding that the ρ_{eff} of electrodeposited Ru is lower than $\rho_{Ru,bulk}$ is independent of whether a Ru nitrosyl sulfate or a Ru chloride salt is used as the Ru metal ion source.

Figure 7 shows a cross-section TEM and HAADF STEM of Ru electrodeposited onto epitaxial Au(111). The layer was electrodeposited at -250 μA/cm^2 from a solution of 2 g/L Ru nitrosyl sulfate and 20 g/L sulfuric acid. The electrodeposited Ru layer is porous, clearly observed in the STEM image, and consists of Ru crystallites. Thus, Ru electrodeposits as a porous layer independent of the seed layer it is deposited onto.

Conclusions

X-ray and S/TEM analyses revealed that the electrodeposited Ru layers were porous with the measured maximum average density ρ_{eff} of the layer never exceeding 80% of the literature value for the density of bulk Ru $\rho_{Ru,bulk}$. Rather than depositing as a fully dense layer, the electrodeposited film is made up of a mixture of nanometer-scale (0001) oriented Ru crystallites and voids. The ability of a metal to electrodeposit epitaxially as a single crystal, then, is not only a factor of the lattice mismatch between the depositing metal and the single crystal seed layer but also of the reduction mechanism of the metal ion and the chemistry of the deposition electrolyte. An increase in nucleation density and surface mobility of Ru atoms may achieve a denser electrodeposited Ru film. While Ru films electrodeposited from solution of Ru nitrosyl sulfate are not suitable as interconnects in ICs, this porosity and large increase in surface area may be beneficial for use as a catalyst. The variations in the electrolyte (Ru metal ion source, solution pH, temperature, agitation), deposition mode (galvanostatic and potentiostatic), and seed layer (polycrystalline Ru, Ru(0001), and Au(111)) that were explored were unable to achieve the electrodeposition of a fully dense, non-porous Ru layer.

Acknowledgments

This material is based on work supported by the Semiconductor Research Corporation (task 2764.001 and 2764.003), the National Science Foundation (ECCS-1740270 and 1740228), and the Air Force Office of Scientific Research (AFOSR FA9550-18-1-0063 and FA9550-19-1-0156). The microscopy for this work was carried out in the Electron Microscopy and Shared Materials Characterization Laboratories of Columbia Nano Initiative (CNI) Facilities at Columbia University. The polycrystalline Ru wafer was provided by Dr. Anniruddha Joi of Lam Research. Cu wafers were provided by Matthew Patrick of the Columbia University Department of Applied Mathematics and Applied Physics.

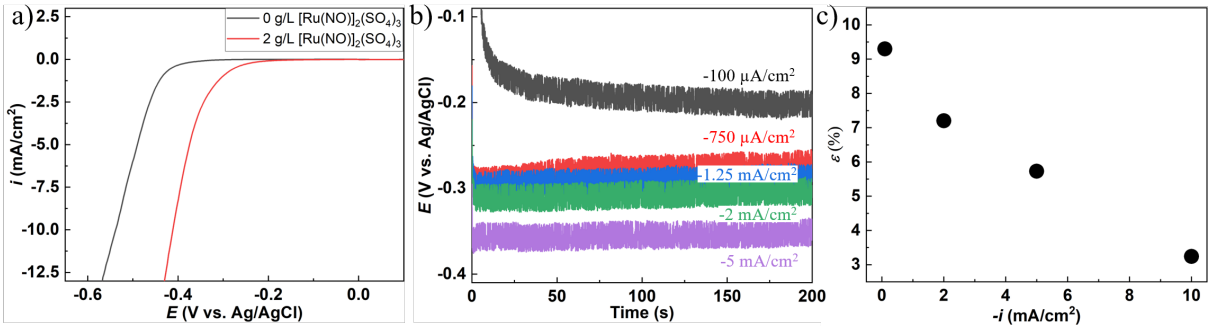

Fig. 1 – (a) LSV collected on a 60 nm-thick Ru(0001) seed layer in 20 g/L H_2SO_4 without (black) and with (red) 2 g/L ruthenium(III) nitrosyl sulfate, scan rate of 2 mV/s, (b) potential transients with a step size of 0.05 s collected on a 60 nm-thick Ru(0001) seed layer in the Ru electrodeposition solution from applied current densities of -0.1 mA/cm^2, -0.75 mA/cm^2, -1.25 mA/cm^2, -2 mA/cm^2, and -5 mA/cm^2, and (c) current efficiency of the Ru electrodeposition reaction as a function of -*i*.

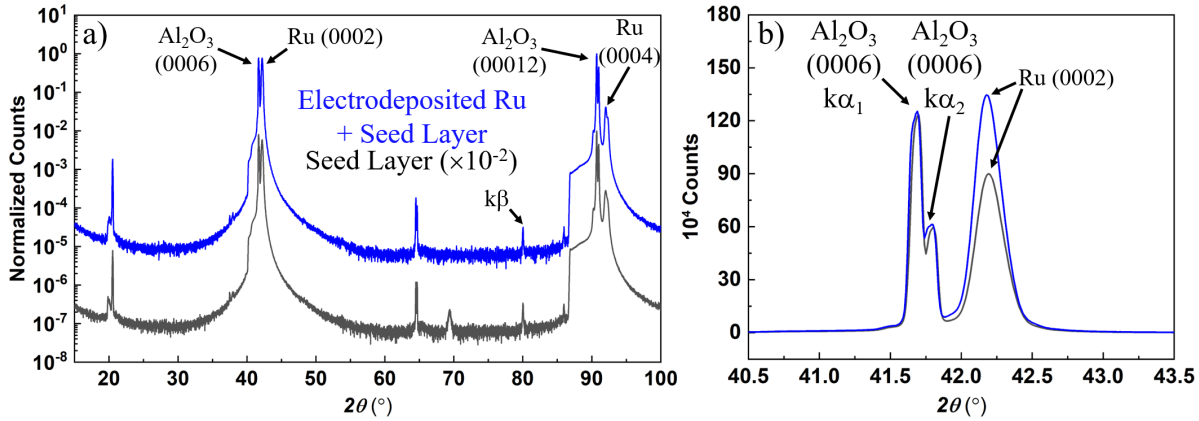

Fig. 2 –Symmetric θ-2θ X-ray diffractograms collected on of the 60 nm-thick Ru(0001) seed layer (black) and the seed layer plus Ru electrodeposited onto 60 nm-thick Ru(0001) at -100 μA/cm^2 for 0.7 C/cm^2 (blue) from (a) 15° to 100° and from (b) 40.5° to 43.5°. The diffractograms in (a) are vertically offset for clarity.

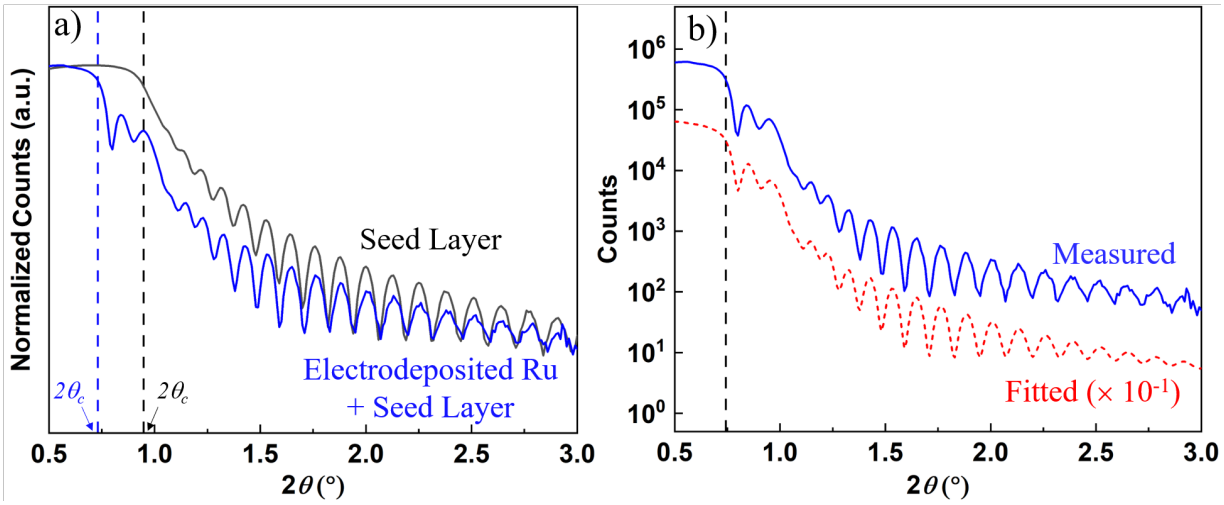

Fig. 3 – (a) X-ray reflectivity (XRR) curves of the 60 nm-thick Ru(0001) seed layer (black) and the seed layer plus Ru electrodeposited onto 60 nm-thick Ru(0001) at -100 μA/cm^2 for 0.7 C/cm^2 (blue), and (b) an XRR curve of Ru electrodeposited at -100 μA/cm^2 for 0.7 C/cm^2 onto 60 nm-thick Ru(0001) (blue) with the corresponding curve fit (red). The curves in (b) are vertically offset for clarity.

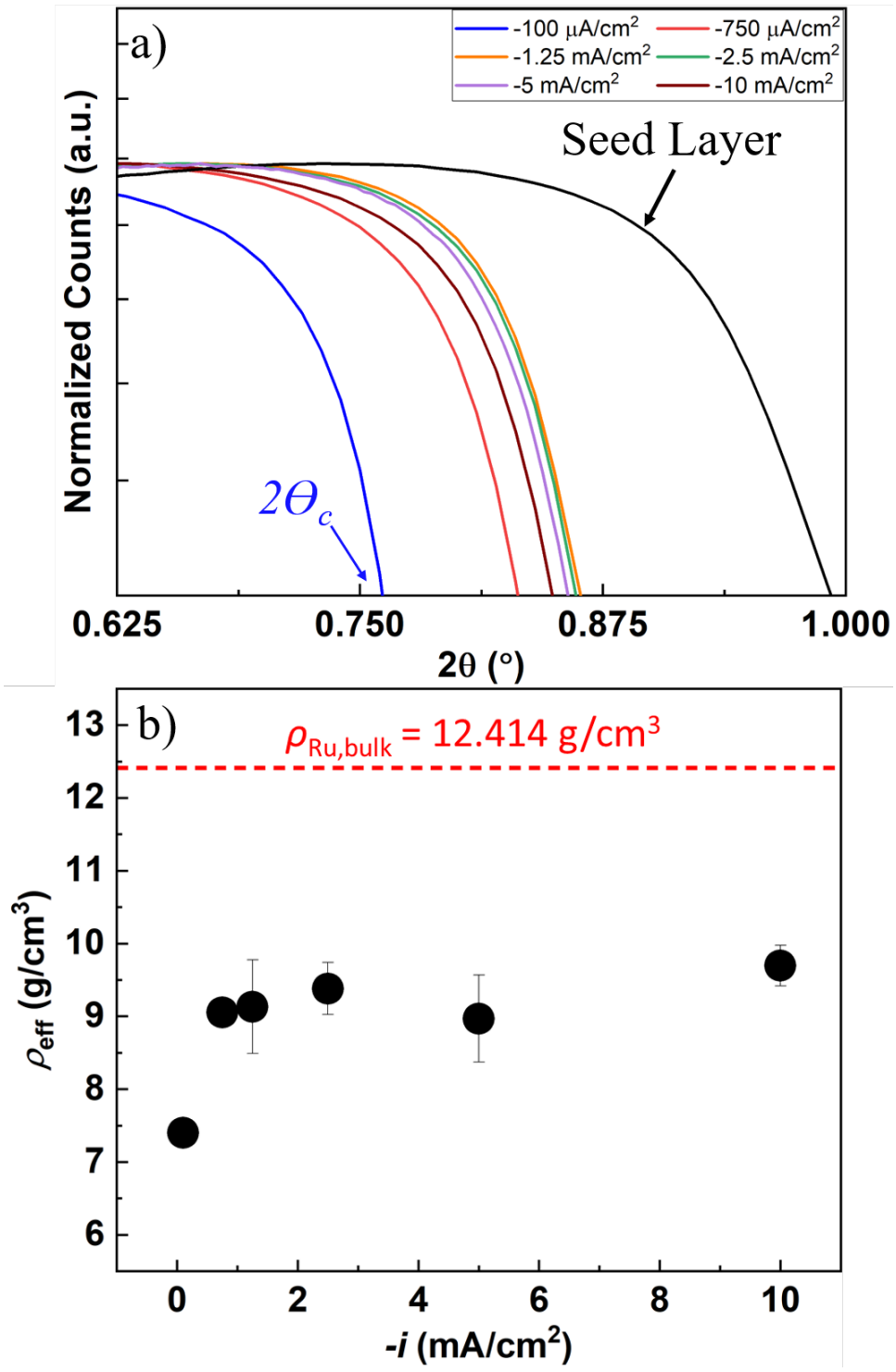

Fig. 4 – (a) XRR curves obtained on a polycrystalline Ru seed layer and the polycrystalline Ru seed layer plus Ru electrodeposited at various current densities for 0.7 C/cm^2 and (b) the calculated ρ_{eff} of electrodeposited Ru films as a function of -*i*. Error bars are not visible at -100 μA/cm^2 and -750 μA/cm^2 as they are smaller than the data point.

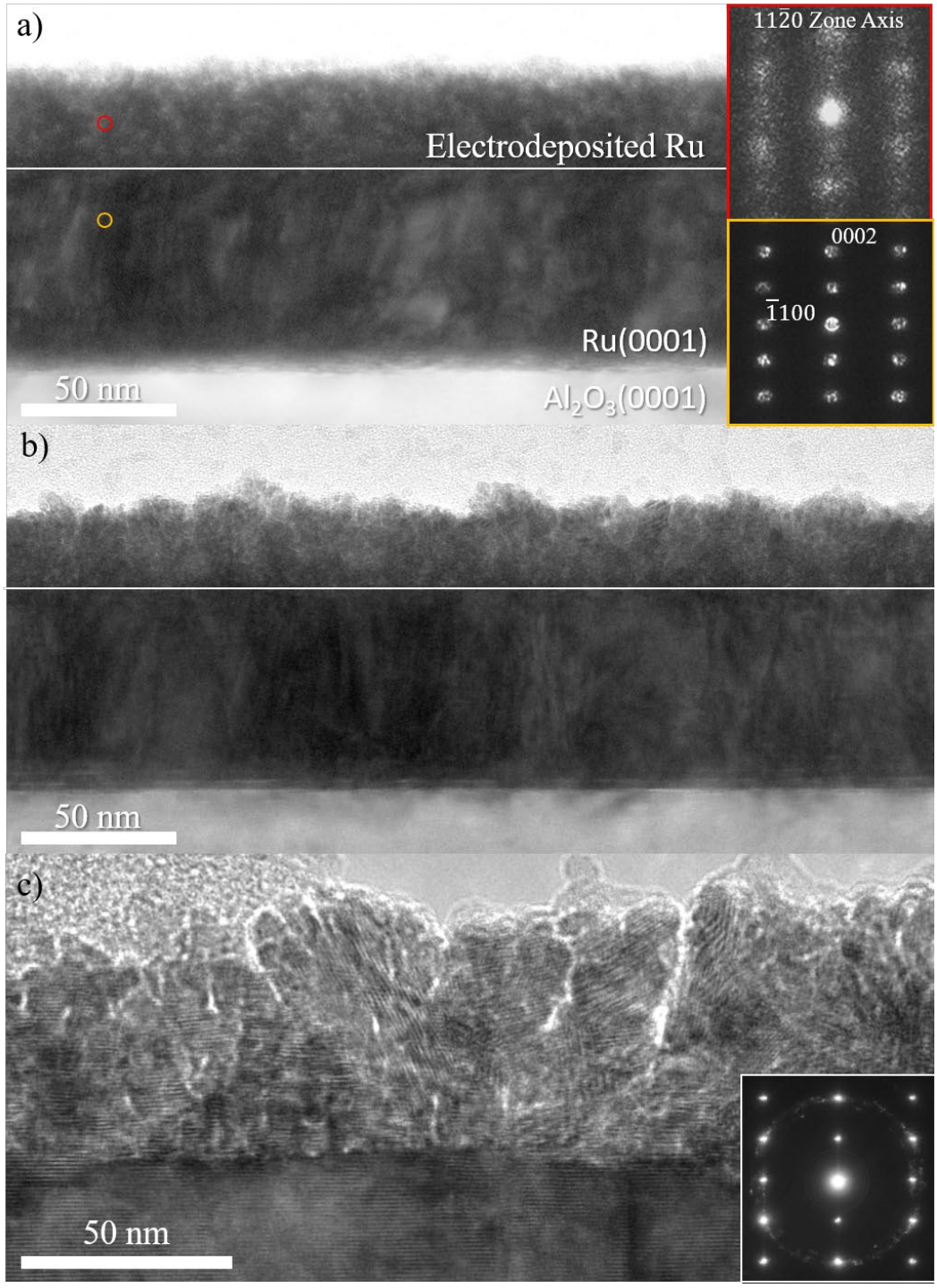

Fig. 5 – Transmission electron micrographs of Ru electrodeposited at (a) -100 μA/cm^2 and (b) -10 mA/cm^2 onto 60-nm thick Ru(0001) and (inset) nanobeam electron diffraction patterns obtained from both the electrodeposited Ru layer and Ru(0001) seed layer. (c) Higher-resolution TEM micrograph of Ru electrodeposited at -10 mA/cm^2 and (inset) electron diffraction pattern obtained from the electrodeposited Ru layer and Ru(0001) seed layer. Kinematically forbidden 0001 and $000\bar{1}$ Ru reflections are present in the electron diffraction pattern from double diffraction.

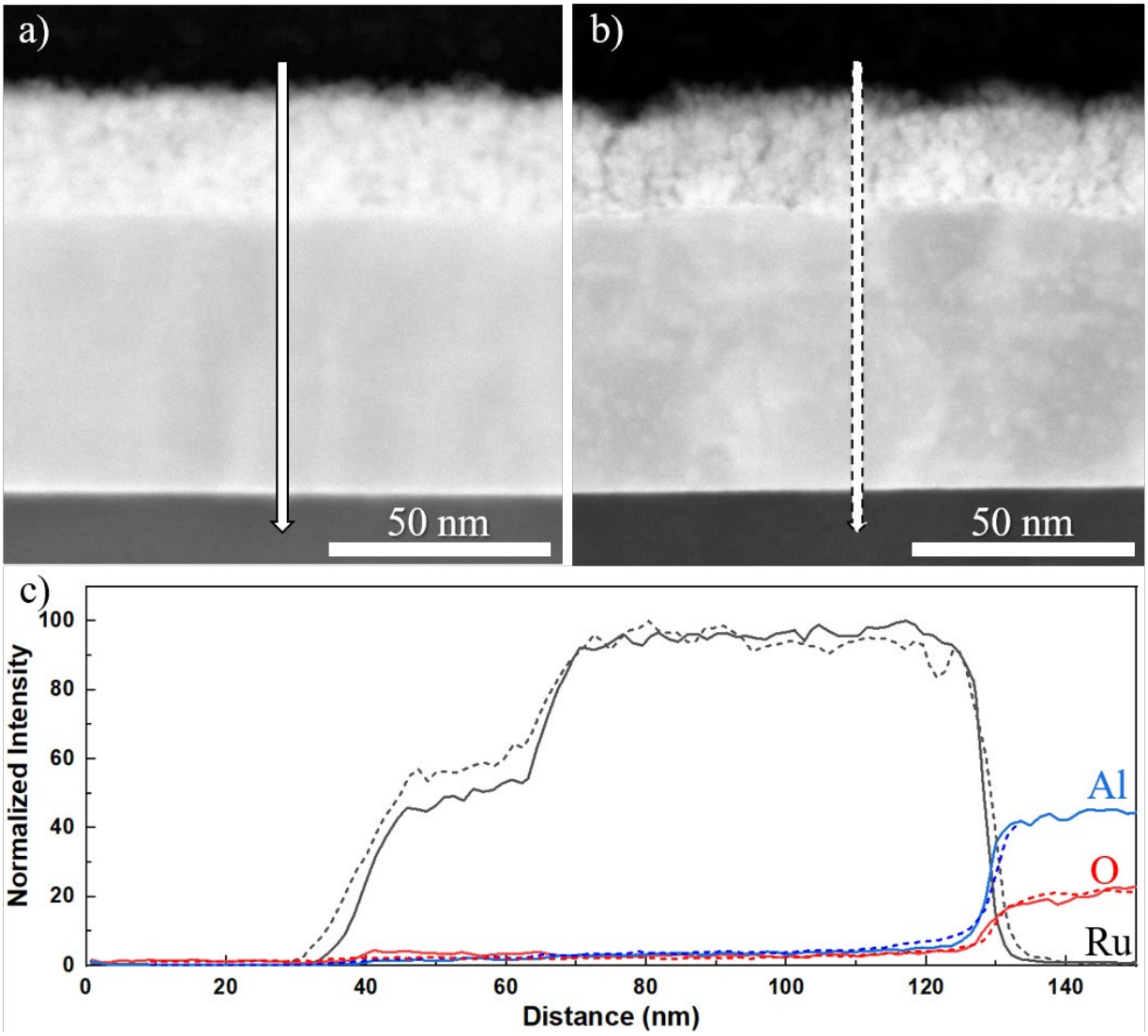

Fig. 6 – High-angle annular dark-field scanning transmission electron micrographs of Ru electrodeposited at (a) -100 μA/cm^2 and (b) -10 mA/cm^2 onto 60-nm thick Ru(0001). (c) EDX line scans performed in the direction of the arrow drawn on the HAADF images, where the solid lines are associated with (a) and the dotted lines are associated with (b).

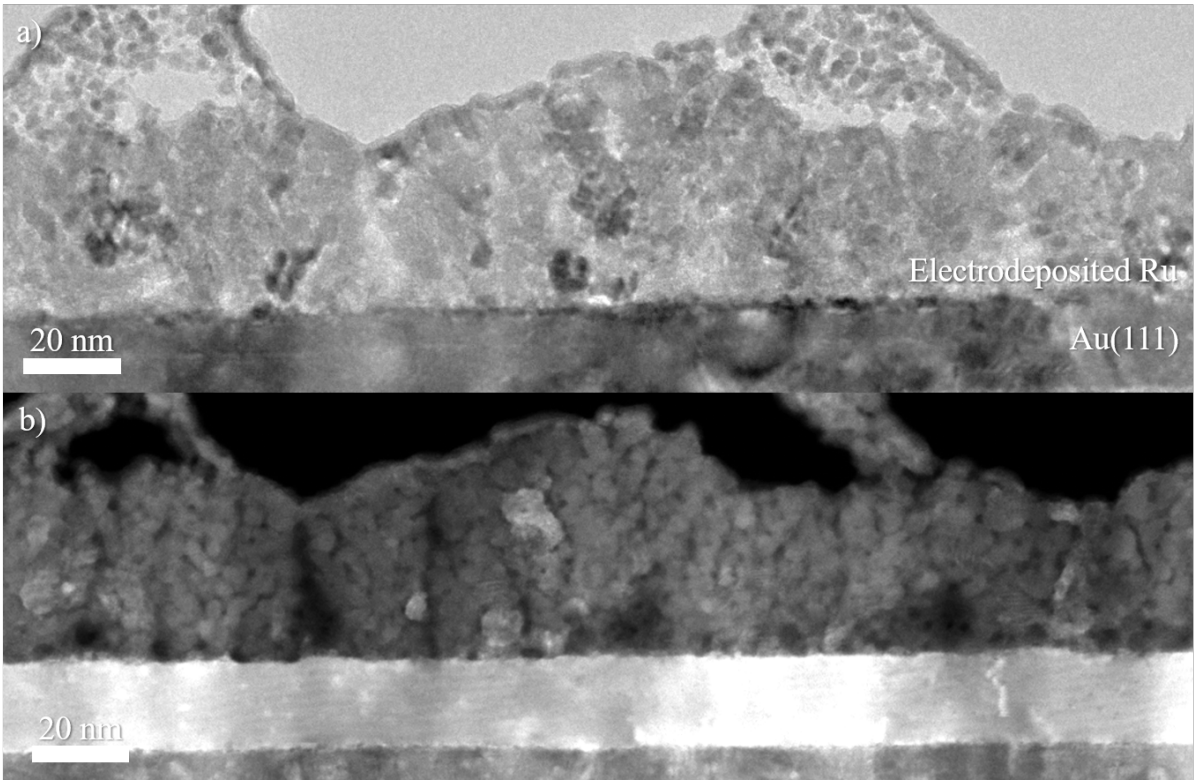

Fig. 7– (a) Transmission electron micrograph and (b) high-angle annular dark-field scanning transmission electron micrograph of Ru electrodeposited at -250 μA/cm^2 for 0.45 C/cm^2 onto 20-nm thick Au(111).

References

1. H. Liu, C. Song, L. Zhang, J. Zhang, H. Wang, and D. P. Wilkinson, *J. Power Sources* **155**, 95 (2006).
2. X. Ren, M. S. Wilson, and S. Gottesfeld, *J. Electrochem. Soc.* **143**, L12 (1996).
3. A. Moura, J. Fajín, M. Mandado, and M. Cordeiro, *Catalysts* **7**, 47 (2017).
4. H. Schulz, *Appl. Catal. A Gen.* **186**, 3 (1999).
5. J. Kothandaraman, A. Goeppert, M. Czaun, G. A. Olah, and G. K. S. Prakash, and Prakash G. K. S., *J. Am. Chem. Soc.* **138**, 778 (2016).
6. R. Bernasconi and L. Magagnin, *J. Electrochem. Soc.* **166**, D3219 (2019).
7. O. Chyan, T. N. Arunagiri, and T. Ponnuswamy, *J. Electrochem. Soc.* **150**, C347 (2003).
8. M. W. Lane, C. E. Murray, F. R. McFeely, P. M. Vereecken, and R. Rosenberg, *Appl. Phys. Lett.* **83**, 2330 (2003).
9. T. P. Moffat, M. Walker, P. J. Chen, J.E. Bonevich, W. F. Egelhoff, L. Richter, C. Witt, T. Aaltonen, M. Ritala, M. Leskelä, and D. Josell, *J. Electrochem. Soc.* **153**, C37 (2006).
10. K. Barmak, S. Ezzat, R. Gusley, A. Jog, S. Kerdsongpanya, A. Khanya, E. Milosevic, W. Richardson, K. Sentosun, A. Zangiabadi, D. Gall, W. E. Kaden, E. R. Mucciolo, P. K. Schelling, A. C. West, and K. R. Coffey, *J. Vac. Sci. Technol. A* **38**, 033406 (2020).
11. S. S. Ezzat, P. D. Mani, A. Khaniya, W. Kaden, D. Gall, K. Barmak, and K. R. Coffey, *J. Vac. Sci. Technol. A* **37**, 031516 (2019).
12. D. Gall, *J. Appl. Phys.* **119**, 085101 (2016).
13. D. Gall, *J. Appl. Phys.* **127**, 050901 (2020).
14. T. Sun, B. Yao, A. P. Warren, K. Barmak, M. F. Toney, R. E. Peale, and K. R. Coffey, *Phys. Rev. B* **79**, 41402 (2009).

15. K. Barmak, X. Liu, A. Darbal, N. T. Nuhfer, D. Choi, T. Sun, A. P. Warren, K. R. Coffey, and M. F. Toney, *J. Appl. Phys.* **120**, 065106 (2016).

16. R. Gusley, K. Sentosun, S. Ezzat, K. R. Coffey, A. C. West, and K. Barmak, *J. Electrochem. Soc.* **166**, D875 (2019).

17. R. Gusley, S. Ezzat, K. R. Coffey, A. C. West, and K. Barmak, *J. Electrochem. Soc.* **167**, 162503 (2020).

18. E. Milosevic, S. Kerdsongpanya, A. Zangiabadi, K. Barmak, K. R. Coffey, and D. Gall, *J. Appl. Phys.* **124**, 165105 (2018).

19. E. Milosevic, S. Kerdsongpanya, M. E. Mcgahay, A. Zangiabadi, K. Barmak, and D. Gall, *J. Appl. Phys.* **125**, 245105 (2019).

20. Y. S. Kim, H. Il Kim, J. H. Cho, H. K. Seo, G. S. Kim, S. G. Ansari, G. Khang, J. J. Senkevich, and H. S. Shin, *Electrochim. Acta* **51**, 5445 (2006).

21. P. Swain, C. Mallika, C. Jagadeeswara Rao, U. Kamachi Mudali, and R. Natarajan, *J. Appl. Electrochem.* **45**, 209 (2015).

22. P. Swain, C. Mallika, R. Srinivasan, U. K. Mudali, and R. Natarajan, *J. Radioanal. Nucl. Chem.* **298**, 781 (2013).

23. F. H. Reid and J. C. Blake, *Trans. IMF* **38**, 45 (1961).

24. M. H. Lietzke and J. C. Griess, *J. Electrochem. Soc.* **100**, 434 (1953).

25. D. K. Oppedisano, L. A. Jones, T. Junk, and S. K. Bhargava, *J. Electrochem. Soc.* **161**, D489 (2014).

26. M. Jayakumar, K. A. Venkatesan, R. Sudha, T. G. Srinivasan, and P. R. Vasudeva Rao, *Mater. Chem. Phys.* **128**, 141 (2011).

27. J. J. Jow, H. J. Lee, H. R. Chen, M. S. Wu, and T. Y. Wei, *Electrochim. Acta* **52**, 2625 (2007).

28. J. N. Crosby, *Ruthenium electroplating and baths and compositions therefor*, US 4,297,178 (1981), United States Patent issued October 27. https://patentimages.storage.googleapis.com/ed/ec/f5/3f4f6e8c785e5e/US4297178.pdf

29. J. N. Crosby, *Electrodeposition of ruthenium*, US 4,082,625 (1978), United States Patent issued April 4. https://patentimages.storage.googleapis.com/e0/1e/31/8fefc1fb621f68/US4082625.pdf

30. G. Reddy and P. Taimsalu, *Electrodeposition of ruthenium*, US 3,576,724 (1971). United States Patent issued April 27. https://patentimages.storage.googleapis.com/7f/21/08/63be345fdc2f69/US3576724.pdf

31. R. Bernasconi, A. Lucotti, L. Nobili, and L. Magagnin, *J. Electrochem. Soc.* **165**, D620 (2018).

32. W. D. Sides and Q. Huang, *J. Electrochem. Soc.* **167**, 062509 (2020).

33. H. Wang, J. Wang, M. Tian, L. Bell, E. Hutchinson, M. M. Rosario, Y. Liu, A. Amma, and T. Mallouk, *Appl. Phys. Lett.* **84**, 5171 (2004).

34. T. Jones, *Met. Finish.* **99**, 121 (2001).

35. U. Emekli and A. C. West, *Electrochim. Acta* **54**, 1177 (2009).

36. L. G. Parratt, *Phys. Rev.* **95**, 359 (1954).

37. D. K. Bowen and B. K. Tanner, *X-Ray Metrology in Semiconductor Manufacturing*, CRC Press, FL (2006) pp. 7-11, 31, 111-127.

38. J. W. Arblaster, *Selected Values of the Crystallographic Properties of Elements*, ASM, (2018).

39. V. K. Kamineni, M. Raymond, E. J. Bersch, B. B. Doris, and A. C. Diebold, *AIP Conf. Proc.* **1173**, 114 (2009).

40. P. Bergese, E. Bontempi, and L. E. Depero, *Appl. Surf. Sci.* **253**, 28 (2006).

41. V. Holy, U. Pietsch, and T. Baumbach, *High-Resolution X-Ray Scattering from Thin Films and Multilayers*, Springer, New York, (2007) pp. 17-37, 120-128.

42. M. Yasaka, *Rigaku J.* **26**, 1 (2010).

43. H. Mimura, H. Ohta, K. Akiba, and Y. Onodera, *J. Nucl. Sci. Technol.* **39**, 655 (2002).

44. A. Sasahira, T. Hoshikawa, M. Kamoshida, and F. Kawamura, *J. Nucl. Sci. Technol.* **33**, 753 (1996).

45. J. O. Bockris and J. Kim, *J. Electrochem. Soc.* **143**, 3801 (1996).

46. C. L. Green and A. Kucernak, *J. Phys. Chem. B* **106**, 1036 (2002).

47. Z. Liu, M. Zheng, R. D. Hilty, and A. C. West, *J. Electrochem. Soc.* **157**, D411 (2010).

48. J. Nutariya, M. Fayette, N. Dimitrov, and N. Vasiljevic, *Electrochim. Acta* **112**, 813–823 (2013).

49. M. A. Rigsby, L. J. Brogan, N. V. Doubina, Y. Liu, E. C. Opocensky, T. A. Spurlin, J. Zhou, and J. D. Reid, *J. Electrochem. Soc.* **166**, D3167 (2019).

50. Q. M. Phung, G. Pourtois, J. Swerts, K. Pierloot, and A. Delabie, *J. Phys. Chem. C* **119**, 6592–6603 (2015).

51. S. Bliznakov, M. Vukmirovic, E. Sutter, and R. Adzic, *Maced. J. Chem. Chem. Eng.* **30**, 19–27 (2011).

52. T. Makino, R. Aogaki, and E. Niki, *J. Chem. Phys.* **81**, 5145–5150 (1984).

53. M. Birkholz, *Thin Film Analysis by X-Ray Scattering*, Wiley-VCH, Weinheim (2006).

54. D. B. Williams and C. B. Carter, *Transmission electron microscopy: A textbook for materials science*, Springer, New York (2009) pp. 257-269.

55. J. Schmitz, *Surf. Coatings Technol.* **343**, 83 (2018).

Supplementary Material:

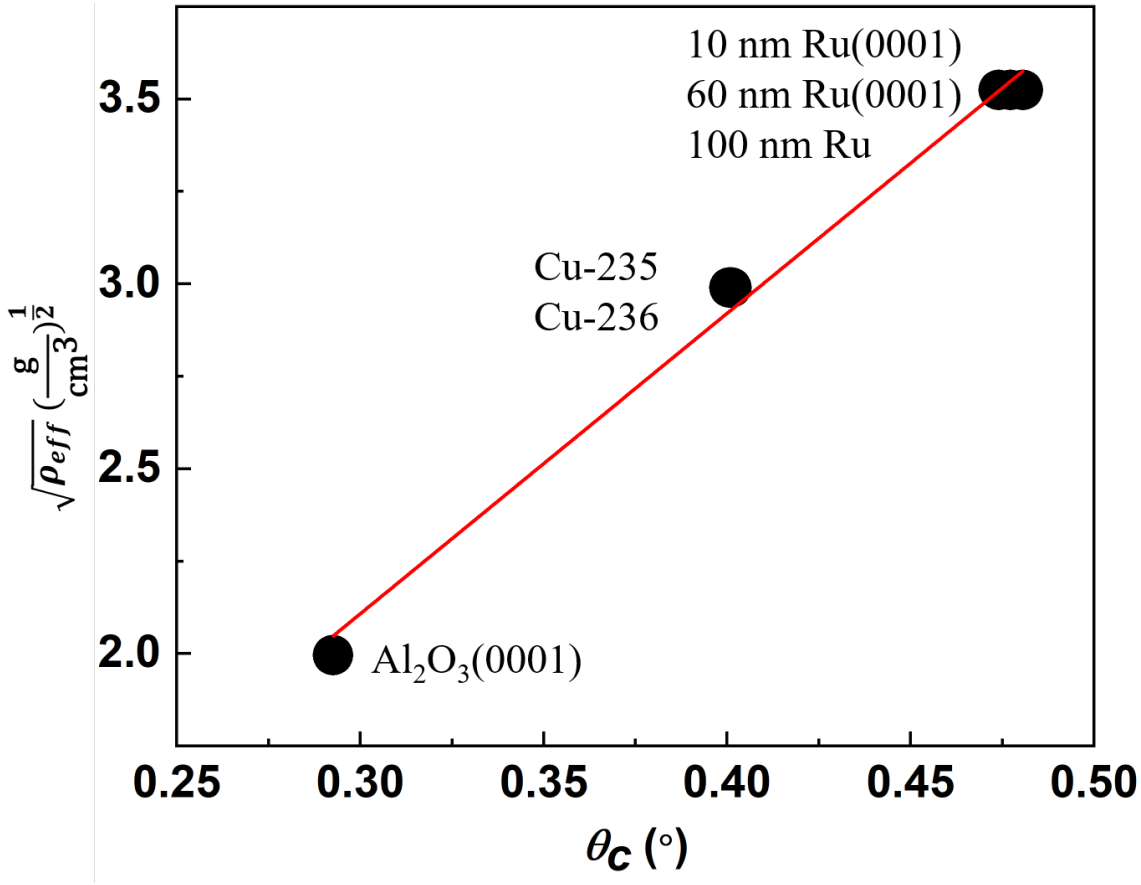

Fig. S1 – XRR calibration curve. The Cu films (Cu-235 and Cu-236) were deposited onto Si(100) by UHV sputter deposition at room temperature with a base pressure in the low 10^{-8} Torr range. The fit results in the following relationship: $\sqrt{\rho_{eff}} = -0.33073 + 8.1252 \times \theta_c$. The R^2 value of the fit is 0.99239.

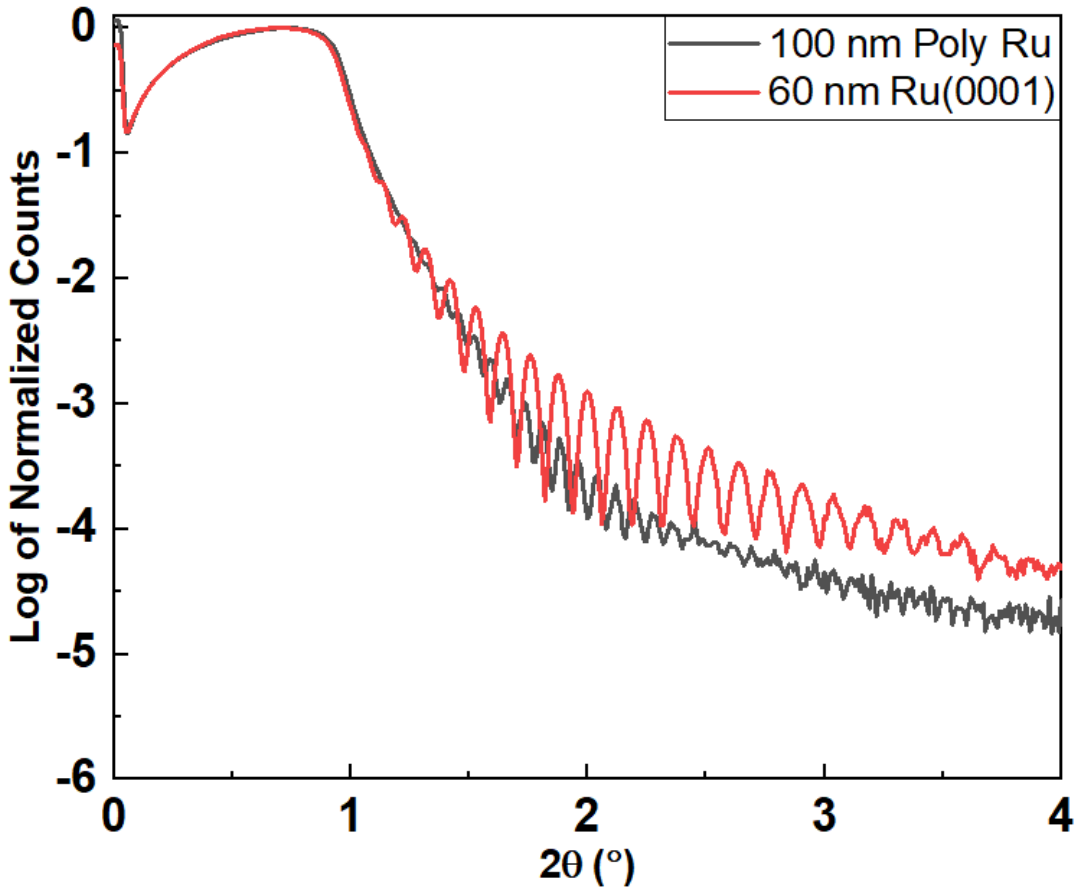

Fig. S2 – XRR curves obtained on 100 nm-thick polycrystalline Ru and 60 nm-thick epitaxial Ru(0001) seed layers.

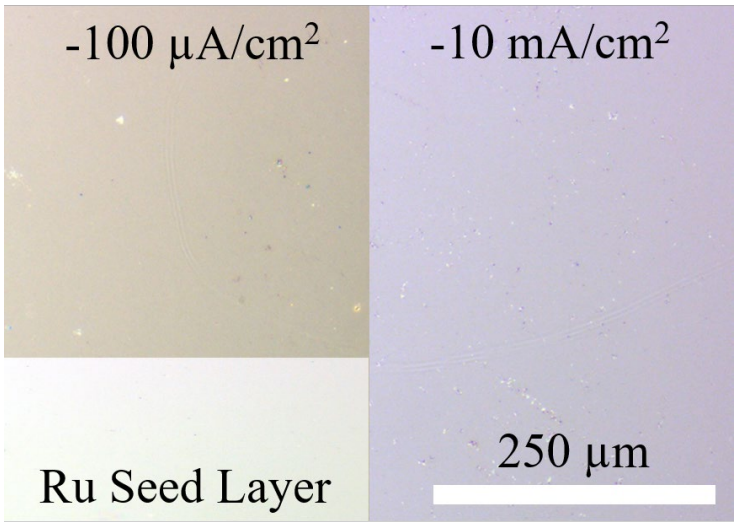

Fig. S3 –Light optical micrographs of Ru electrodeposited at -100 µA/cm^2 (left) and -10 mA/cm^2 (right) onto 60 nm-thick Ru(0001) for a charge density of 0.7 C/cm^2 along with the 60 nm-thick Ru(0001) seed layer prior to Ru electrodeposition (inset).

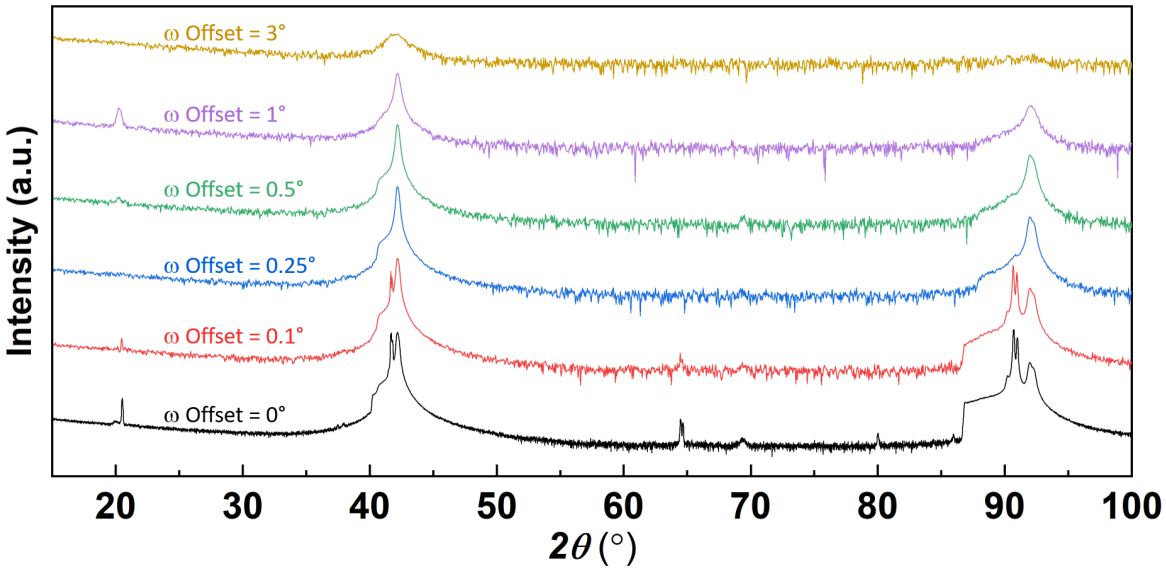

Fig. S4 –Symmetric θ-2θ X-ray diffractogram collected on 60 nm-thick Ru(0001) seed layer from 15° to 100° with a changing ω offset. The scans are vertically offset for clarity.